RSC Advances

ROYAL SOCIETY OF CHEMISTRY

www.rsc.org/advances

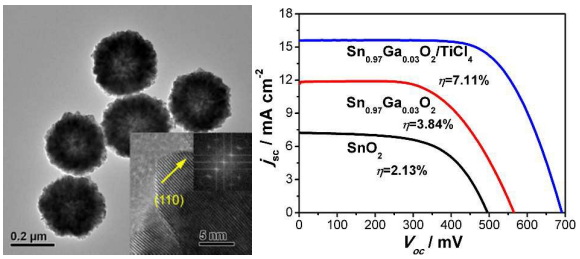

By introducing the rough hollow microspheres structure and Ga-doping technique, a high power conversion efficiency (η) up to 7.11% is obtained for SnO_2 based DSSCs.

Effects of Ga doping and hollow structure on the band-structures and photovoltaic properties of SnO_2 photoanode dye-sensitized solar cells

Yandong Duan,‡[ab] Jiaxin Zheng,‡[a] Nianqing Fu,[bc] Jiangtao Hu,[a] Tongchao Liu,[a] Yanyan Fang,[b] Qian Zhang,[a] Xiaowen Zhou,[b] Yuan Lin*[ab] and Feng Pan*[a]

[a]School of Advanced Materials, Peking University Shenzhen Graduate School, Shenzhen 518055, China

[b]Beijing National Laboratory for Molecular Sciences, Key Laboratory of Photochemistry, Institute of Chemistry, Chinese Academy of Sciences, Beijing 100190, China

[c]Department of Applied Physics, The Hong Kong Polytechnic University, Hung Hom, Kowloon, Hong Kong, China

[d]State Key Laboratory for Advanced Metals and Materials, School of Materials Science and Engineering, University of Science and Technology Beijing, Beijing 100083, China

‡These authors contributed equally to this work.

*Corresponding author: linyuan@iccas.ac.cnTel: 86-10-82615031 Fax: 86-10-82617315

*Corresponding author: panfeng@pkusz.edu.cnTel: 86-755-26033200

Abstract:

The photon-to-electricity conversion properties of the prepared photoanode based on SnO_2 nanocrystals, which are assembled as the rough hollow microspheres (RHMs), are improved by aliovalent Ga^{3+} doping. The conduction band (CB) of the doped SnO_2 shifts negatively with increasing the Ga content from 1 to 5 mol% gradually. Moreover, the prepared Ga-doped SnO_2 photoanode shows an advantage in repressing the charge recombination. As a result, both the negative shift of the CB and repressed charge recombination enhance the open-circuit photovoltage (V_{oc}) and the short-circuit photocurrent (J_{sc}) of the DSSCs, and the power conversion efficiency (η) is increased by 80% at 3 mol% Ga-doping SnO_2 to compare with the undoped SnO_2 for DSSCs (AM 1.5, 100 mW cm^{-2}). After treating the samples with $TiCl_4$, an overall photoconversion efficiency (approximately 7.11 %) for SnO_2 based DSSCs is achieved.

Keywords: dye-sensitized solar cell, tin dioxide, Ga-doping, charge recombination

Introduction

As the next generation solar cells, DSSCs have received much attention because of their low costs, chemical stability, and convenient fabrication.[1,2] Many efforts to improve the energy-conversion efficiency (η) of DSSCs have been focused on the improvement of the photoanode, dye, electrolyte, cathode, their interfaces, and the fabrication technologies. So far the highest energy conversion efficiencies ($>$12%) have been achieved with nanocrystalline anatase TiO_2 photoanode.[3] However, further improvement in the photovoltaic performance is limited because of its low electron mobility ($1<cm^2\,V^{-1}\,S^{-1}$) and transport properties.[4] As a result, to seek new alternative photoanode materials, other metal oxide semiconductors such as ZnO,[5] SnO_2,[6,7] $SrTiO_3$,[8] and Zn_2SnO_4[9] have been investigated recently as promising photoelectrodes for DSSCs.

Especially, nanostructured SnO_2 has been considered as an ideal and important substitutive material because of its higher electron mobility (125-250 $cm^2\,V^{-1}\,S^{-1}$) and photostability to compare with those of TiO_2. However, the cell performance of SnO_2-based DSSCs is still far from satisfactory due to the following drawbacks,[10] such as that (1) the more positive (ca. 300 mV) conduction band edge of SnO_2 compared with TiO_2 leads to faster interfacial electron recombination, (2) the lower isoelectric point (pI: 4–5) of SnO_2 compared with anatase TiO_2 (pI: 6–7) results in less adsorption of the dye.[11] Developing effective methods to overcome the above drawbacks would improve the energy conversion efficiency of SnO_2 based DSSCs greatly, such as downsizing the particle size to the nanoscale to increase the specific surface area for more dye loading and surface treatment to repress the interfacial electron recombination.[12-15] Table S1 shows a comparison for different methods (morphology controlling, metal doping, surface coating, etc.) to improve the photovoltaic performance of the SnO_2 based DSSCs.[11, 12, 16-24]

Doping metal atoms into photoanodes is a widely adopted method to tailor their properties, such

as the electrical conductance, conductance band position, charge recombination rates, and trap/defect level distribution.[25-27] For example, it is reported that Nb-doped TiO_2 and the Nb doping can lead to a significant increase of powder conductivity and a positive shift in the V_{fb}.[28] Mg-doping in SnO_2 can reduce the charge recombination and prolong the electron lifetime in DSSCs device.[13] Teng et al. reported that the density of empty trap states for electron localization is smaller for the Zn-doped TiO_2 films relative to that of the bare-TiO_2 film due to increased band bending resulting from the elevated electron Fermi level.[29] Ga-doped SnO_2 has been applied in photocatalysis, resulting in an increase in the photocurrent and photovoltage compared with non-doped SnO_2. However, there is no detailed study about the mechanism of electron lifetime and electron transport in the Ga-doped SnO_2 samples, and the overall photoconversion efficiency is unsatisfactory (4.05 %).[30] Heterovalent substitution is an effective approach to directly affect the Fermi level and further increase the carrier concentration. In a previous work of ours,[31] we reported that both tuning the conduction band and suppressing the charge recombination are synchronously improved in the Al^{3+}-doped SnO_2 photoanode, and a high energy-conversion efficient of 6.91% for Al-doped SnO_2 DSSCs can be easily obtained. Analogously, Ga^{3+} doping is also anticipated to improve the performance of SnO_2 based DSSCs.

Moreover, to further improve the performance of SnO_2 based DSSCs, the electrode structrue should be modified. Nanostructured hollow spheres have been demonstrated to be efficient materials because of their low density, high specific surface area, light scattering ability and densely packed microstructure for fast electron transport. In this work, the Ga-doped SnO_2 nanocrystals to self-assemble as rough hollow microspheres (RHMs) photoanodes for DSSCs were prepared by the hydrothermal method. The doped SnO_2 samples with Ga show both improvements of significant reduction of the electron recombination and optimization of the band structure. With a $TiCl_4$ post

treatment, the high overall photoconversion efficiency of approximately 7.11% for DSSCs based on Ga-doped SnO_2 is achieved, which is over 2 times higher than that of pure SnO_2 samples. This value is not only larger than that for our previous Al-doped SnO_2 DSSCs (6.91 %) but also one of the highest so far to compare with the other reported high values for SnO_2 based DSSCs (Table S1). Finally, the mechanism behind the improvement by Ga-doping was discussed by the experimental measurements and the density functional theory (DFT) calculations.

Experimental section

Materials

$SnCl_2 \cdot 2H_2O$ (AR, Sinopharm Chemical Reagent Co., Ltd.), $Ga(NO_3) \cdot 9H_2O$ (99.9%, Alfa), LiI (AR, Acros), I_2 (AR, Acros), and 4-tert-butylpyridine (TBP, AR, Aldrich) , 3-methoxypropionitrile (MPN, 99%, GC, Alfa) were commercially available. All the chemicals were used without further purification. 3-Hexyl-1-methylimidazolium iodide was prepared according to the literature.[32] The electrode substrate is fluorine-doped tin oxide conducting glass (FTO, Nippon Sheet Glass; thickness, 2.2 mm; sheet resistance, 14 Ω/square).

Synthesis of SnO_2 and Ga-doped SnO_2

The pure SnO_2 rough hollow microspheres were synthesized according to the literature.[21] In a typical synthesis process, 3 mL of concentrated hydrochloric acid (37.5 wt%) was added to ethanol/distilled water (165 ml, 30/3, v/v). The mixture was stirred under ambient conditions for 3 min before 0.75 g of $SnCl_2 \cdot 2H_2O$ was added. Then the turbid precursor was stirred for 60 min. The resulting solution was transferred to a Teflon-lined stainless steel autoclave of 200 mL volume and kept in an air-flow electric oven at 200 ℃ for 24 h. Afterward, the autoclave was taken out to cool down naturally. The white precipitate was then harvested by centrifugation and washed thoroughly

with ultrpure water before drying at 80 °C overnight. For preparing of the Ga-doped samples, $Ga(NO_3)\cdot 9H_2O$ and $SnCl_4\cdot 5H_2O$ was added to ethanol/distilled water (molar ratio of Ga and Sn were 1:99, 3:97 and 5:95) to start the hydrothermal process. The obtained samples was denoted as SnO_2, $Sn_{0.99}Ga_{0.01}O_2$, $Sn_{0.97}Ga_{0.03}O_2$ and $Sn_{0.95}Ga_{0.05}O_2$.

Cell fabrication and photovoltaic measurements

SnO_2 and Ga-doped SnO_2 films (ca. 8-9 μm) were fabricated on the FTO substrates using a doctor-blade method and the electrodes were sintered at 450 °C for 30 min. $TiCl_4$ surface treating is conducted by dipping the photoanodes in 40 mM $TiCl_4$ aqueous solution at 70 °C for 30 min and then sintering under 500 °C. After the heating, when the temperature cooled to 80 °C, the electrodes were immersed in a dye bath containing 0.5 mM cis-$Ru(H_2dcbpy)_2(NCS)_2$(H_2dcbpy = 4,4′-dicarboxy-2,2′-bipyridyl) (N3) in ethanol for 24 h. The film thickness was measured by SEM. Then, the N3-loaded electrode was assembled with the prepared Pt counter electrode to form a sandwich-type DSCs. A drop of electrolyte solution (composition: 0.5 M LiI, 0.05 M I_2, 0.6 M TBP, and 0.6 M HMII in MPN) was added between the two electrodes of the cell. The photovoltaic performance was measuredusing a Keithly 2611 Source Meter (Keithley Instruments, Inc.). The light source was a AM 1.5 solar simulator (91160A, Newport Co.). The incident light intensity (100 mW cm^{-2}) was adjusted with a standard Silicon reference solar cell and and the cell active area was 0.20 cm^2.

Characterization

The crystalline phase was confirmed using high-power X-ray diffraction (XRD, Rigaku D/MAX 2500 V diffractor) with Cu Kα radiation. High-resolution transmission electron microscopy (HR-TEM,Tecnai G2 20 S-TWIN) was used to examine the morphology and mesopore structures.

X-ray photoelectron spectroscopy (XPS) measurements were performed using an Al Kα radiation (1486.6 eV) (ESCALab220i-XL, VG Scientific) at ~3×10^{-9} mbar background pressure. The binding energies are calibrated by C1s photoelectron peak (284.8eV). A three-electrode system was employed for measuring Mott-Schottky plots with SnO_2 or Ga-doped SnO_2 films (without dyes, ca. 3 μm) as a photoanode, an saturated calomel electrode (SCE) and a platinum wire as reference electrode and counter electrode, respectively. The active area was 0.25 cm^2. SnO_2 or Ga-doped SnO_2 films (ca. 3μm) adsorbed by dyes were used for the EIS, IMPS, and IMVS test. Electrochemical impedance spectroscopy (EIS) measurements were carried out with Solartron 1255B frequency analyzer and Solartron SI 1287 electrochemical interface system (light intensity: 100 mW cm^{-2}). IMPS and IMVS were obtained using a green light emitting diode (max = 520 nm) driven by a solartron 1255B frequency-response analyzer. The LED provided both the dc and ac components of the illumination. The specific resistivity were conducted using a four-probe technique (KDY-1, Kunde Technology)

Computational details

In order to model the SnO_2 doped by Ga, a 2×2×2 supercell (48 atoms) based on the unit cell was constructed, allowing us to investigate different substitution degrees of $Sn_{1-x}Ga_xO_2$. All calculations are performed using the generalized Kohn-Sham theory with the screened hybrid functional of Heyd, Scuseria, and Ernzerhof(HSE)[35,36] as implemented in the Vienna ab initio simulation package[37,38]. Compared with conventional functionals such as PBE and PBE0, the HSE hybrid functional can produce more close results to experimental values, such as lattice constants, band gaps, and formation enthalpies.[39] In this approach, a fraction of Hartree-Fock (HF) exchange potential is mixed with the exchange potential of the Perdew-Burke-Ernzerhof (PBE)[40] form of generalized gradient approximation (GGA). Here the HF mixing parameter was set to 0.32 to yield good agreement with

the experimental bandgap of SnO_2.[41] To obtain reliable optimized structures, the maximum residual force is less than 0.01 eV/Å and energies are converged to within 5×10^{-6} eV per atom. The k-point mesh is set to 2×2×2 to calculate electronic properties. An energy cut-off of 450 eV was used in all cases.

We first calculated the formation energies for the doping site of substituting a Sn atom and a interstitial site, respectively. Here, we calculate the formation energy of a Sn atom substituted by a Ga atom using the following formula:

$$E^f(Ga^{Sn}) = E_{tot}(Ga^{Sn}) + \mu_{Sn} - E_{tot}(bulk) - \mu_{Ga} \quad (1)$$

The formation energy of a Ga interstitial doping is calculated as:

$$E^f\left(Ga^{int}\right) - E_{tot}\left(Ga^{int}\right) - E_{tot}(bulk) - \mu_{Ga} \quad (2)$$

Where E_{tot} (Ga^{Sn}), E_{tot} (bulk), and E_{tot} (Ga^{int}) are, respectively, the total energies of a supercell in which a Sn atom has been substituted by a Ga atom, a supercell of the perfect bulk SnO_2 material, and a supercell of a Ga interstitial doping; $?_{Sn}$ and $?_{Ga}$ are, respectively, the atomic chemical potentials of species Sn and Ga (referenced to the standard state). The chemical potentials depend on experimental conditions and sources of impurities and can be estimated from experimental formation enthalpies. We can compare the $E^f(Ga^{Sn})$ with $E^f\left(Ga^{int}\right)$ by using Eq. (1) minus Eq. (2):

$$E^f(Ga^{Sn}) \quad E^f\left(Ga^{int}\right) = [E_{tot}(Ga^{Sn}) \quad E_{tot}\left(Ga^{int}\right)] \; \mu_{Sn} \quad (3)$$

Based on our calculation results, we can get $E^f(Ga^{Sn}) - E^f\left(Ga^{int}\right)$ to be (3.79 eV + μ_{Sn}), which depends on the chemical potential of Sn. To simulate experimental synthesis conditions, we assume that Sn potential μ_{Sn} depends on oxygen pressure in the synthesis system.[42] In our calculations for the oxygen-rich limit, $\mu_{Sn} = \mu_{Sn(metal)} + \Delta H_{SnO_2}$, and for the oxygen-poor limit, $\mu_{Sn} = \mu_{Sn(metal)}$. Here $\mu_{Sn(metal)}$ is calculated to be -4.009 eV, thus we can get $E^f(Ga^{Sn}) - E^f\left(Ga^{int}\right)$ to be -0.21 eV at the oxygen-poor limit. For the oxygen-rich limit, because ΔH_{SnO_2} is negative, $E^f(Ga^{Sn}) - E^f\left(Ga^{int}\right)$ will still be negative. As a result, compared with Ga doping at an interstitial, Ga substituting Sn atom will be energy favorable. This is also supported by the XRD results, which

shows that the lattice constants decrease after Ga doping. The DFT calculations show that the lattice constants of SnO_2 would increase after Ga interstitial doping (Table S2), which contradicts the XRD results. By contrast, the lattice constants of SnO_2 would decrease after Ga substituting Sn atoms (Table S2), consistent with the XRD results.

Additionally, because the absolute position of energy levels in a bulk calculation is ill-defined by DFT calculations, here we pick the deep core levels of a Ga atom (far from the doped Ga atom, see red cycled atom in Fig. 7a) to align the energy levels in different calculations.

Results and discussions

The XRD patterns of Ga-doped SnO_2 calcined at 450□ in air for 30 min are presented in Fig. 1(a). All of the undoped and the Ga-doped SnO_2 have a tetragonal rutile crystal structure (PDF No.77-0448) and no other crystalline forms are detected. As can be seen in the inset of Fig. 1(a), the diffraction peaks shift to higher theta values with increasing Ga^{3+} content to reveal a narrowing of the lattice constant in accordance with the Bragg equation: $2d \sin \theta = \lambda$, which can be attributed to the substitution of Sn^{4+} by Ga^{3+} because of the smaller effective radius of Ga^{3+}(0.62 Å) compared to that of Sn^{4+}(0.69 Å). In Fig. 1(b), the sizes of the SnO_2 nanoparticles, as calculated by the Scherrer equation, decline from 15.85 nm to 13.79 nm as the amount of Ga^{3+} ions increases from 1 to 5 mol%. This is similar to the Al-doping cases, as the average diameter size of SnO_2 decreases from ca. 16 nm to ca. 12 nm after the Al-doping.

The morphologies of the samples are studied by SEM as shown in Fig. 2(a) and (b). The as-synthesized SnO_2 and $Sn_{0.97}Ga_{0.03}O_2$ samples demonstrate the aggregated uniform hollow structure with a diameter of about 300 nm. These hollow nanospheres are assembled with SnO_2 or $Sn_{0.97}Ga_{0.03}O_2$ nanoparticles with shell thickness of about 80-100 nm confirmed by high-resolution

TEM, as shown in Fig. 2(c) and (d). These morphologies are different from the hydrothermal synthesized Al-doped SnO_2 nanoparticles, which show little aggregation. The HRTEM images show lattice fringes with regular spacings of 0.34 nm, which are associated with the (110) planes of SnO_2 and $Sn_{0.97}Ga_{0.03}O_2$. The well resolved fringes indicate that the SnO_2 and $Sn_{0.97}Ga_{0.03}O_2$ nanocrystals possess the high crystallinity.

The binding energies of SnO_2 and $Sn_{0.97}Ga_{0.03}O_2$ samples were referenced to the C1s (284.8 eV) line measured by the XPS spectra (Fig. 3). The tin core levels Sn3$d_{5/2}$ and Sn3$d_{3/2}$ are observed at 486.05 and 494.50 eV, respectively, with a peak-to-peak separation of 8.45 eV. Compared with the pure SnO_2 sample, a slight negative shift in binding energy was found from the $Sn_{0.97}Ga_{0.03}O_2$ samples. The charge transfer occurring between two cationic species has been well studied with XPS for many mixed oxides, where the metallic ions are mixed at an atomic level, forming a heterogeneous linkage of M(A)-O-M(B) (where M(X) represents different metallic species). The electron cloud will be transferred from one type of cation to the other through their oxygen bridge in the linkage structure due to the different cation charge and electronegativity.[43-44] In this case, the binding energy shift arises from electron transfer from Ga to Sn due to the differences of their electron negativity (electron negativity: Sn= 1.96, Ga = 1.81). The positions of Ga2$p_{1/2}$ and Ga2$p_{3/2}$ peaks are at 1118.1 and 1145.1 eV, respectively. These positions are in good agreement with the values previously reported by Schön, suggesting that Ga exists in the form of Ga^{3+}.[45]

Fig. 4(a) shows the current density (J)-voltage (V) curves of DSSCs with the undoped SnO_2 and Ga-doped SnO_2 as the work electrode materials under simulated AM 1.5G illumination (100 mW cm^{-2}). The photovoltaic performances, including the open circuit voltage (V_{oc}), photocurrents (J_{sc}), fill factor (FF), and PCE, are summarized in Table 1. Although loading with less amount of dye, SnO_2 nano hollow DSSC exhibits a higher efficiency than the DSSC based on SnO_2 nanocrystal. The

nano hollow SnO_2 can enhance the light harvesting efficiency due to a higher light scattering ability than the SnO_2 nanocrystal (Figure S2)[46-47]. Additionally, we can see that both V_{oc} and J_{sc} are improved after Ga-doping, and the Ga-doped SnO_2 electrodes showed a better performance than those of undoped SnO_2 nano hollow spheres. The observed shifts of the flat band potential for the samples doped with 1 and 3 mol% of Ga are in agreement with the V_{oc} variation. For the samples doped with 5 mol % of Ga, the decrease of the photovoltaic characteristics of the DSSCs is attributed to the decrease of the electrical conductance of the SnO_2 films (Figure S3). And the overall performance of the films decrease due to the introduction of too many impurities. On the other hand, J_{sc} can be influenced by the light-harvesting efficiency, electrons injection rate, and charge recombination process. The light harvesting efficiency is a strong function of the dye loading. The J_{sc} factor for the given dye and cell design can be determined by: $J_{sc} = \int_{\lambda} \mathrm{LHE}(\lambda)\Phi_{inject.}\eta_{collect.}\mathrm{d}\lambda$. As shown in Table S2, the dye loading amount increases with the increasing doping content (mainly due the the increasing of specific surface area, Table 2)，which partially contributed to the J_{sc} enhancement. According to the Katoh's report,[48] the injection efficiency from excited N3 dyes to the conduction band of SnO_2 are very high, suggesting that the injection process is not a limiting process for J_{SC}. Therefore, to improve the charge collection efficiency will be the additional approach to increasing J_{SC} (which will be discussed later). To further improve the performance of the DSSCs, we treated the electrode films with $TiCl_4$. When $TiCl_4$ modifies the photoanode films, the performance of DSSCs is optimized and the efficiency of the $Sn_{0.97}Ga_{0.03}O_2$ photoanode reaches up to 7.11%, which is larger than that for our previous Al-doped SnO_2 DSSCs (6.91 %) and one of the highest so far to compare with the other reported high values for SnO_2 based DSSCs (Table S1). The photovoltaic parameters are indicated in Table S2 to compare with the DSSCs with and without $TiCl_4$ treatment.

The charge transfer and recombination behavior in the SnO_2 and Ga-doped SnO_2 films was studied by analyzing the EIS spectra at open circuit voltage and the Nyquist plots as shown in Fig. 5. The EIS spectra are characterized by the presence of two semicircles in a Nyquist plot. The high frequency semicircle is resulted from the charge transfer resistance (R_{ct}) at the interfaces of the electrolyte/counter electrode, while the low frequency one is related to the chemical capacitance of SnO_2 and the charge recombination resistance (R_{rec}) between SnO_2 and the electrolyte. We found that the R_{rec} increased with the raising Ga-doping content in SnO_2 films, which resulted in the highest J_{sc} and V_{oc} achieved for the Ga-doped cells.

To further analyze the dynamics of electron transport and charge recombination of the DSSCs, intensity-modulated photocurrent spectroscopy (IMPS) and intensity-modulated photovoltage spectroscopy (IMVS) are performed as shown in Fig. 6. The IMVS shows that the lifetime or recombination time (τ_n) of the Ga-doped SnO_2 is larger than that of the undoped SnO_2, which is indicative of the higher photovoltage of the Ga-doped SnO_2 than that of undoped SnO_2, in agreement with the results of EIS measurement. This result is similar to the Al-doping cases, which also show an enlarged electron lifetime, but the degree is a little smaller for Ga-doping, indicating a more effective charge recombination suppression for Al-doping. However, the transport time (τ_d) of the Ga-doped SnO_2 based cells increases with the increasing Ga-doping content, indicating a more slowly electron transport than that of the undoped SnO_2 based cell. The increased τ_d after Ga-doping is similar to that for the Al-doping cases, but the increasing degree is slighter for Ga-doping. The τ_d increases from 17.9 ms to 40 ms when the Al content increases from 0 to 3 mol%, but the τ_d only increases from 15.2 ms to 21.1 ms when the Ga content increases from 0 to 5 mol%. The charge collection efficiency (η_{cc}) was introduced to quantitative analysis of the effect of transport time and electron lifetime. The η_{cc} of the DSSCs can be calculated according to the relation: $\eta_{cc}=1-(\tau_d/\tau_n)$. The

obtained η_{cc} value for SnO_2, $Sn_{0.99}Ga_{0.01}O_2$, $Sn_{0.97}Ga_{0.03}O_2$, and $Sn_{0.95}Ga_{0.05}O_2$ were 95.9%, 97.2%, 98.1%, and 97.8%, respectively. Thus, the higher η_{cc} value for Ga-doped SnO_2 cells can result in a higher short circuit current (J_{sc}) density than that of the undoped SnO_2 for DSSCs.

Density functional theory (DFT) calculations were performed for our materials to explore the effect of Sn atoms partially substituted by the Ga atoms. Fig. 7a shows the doping model. For each *x* value, we have considered at least four substitution structures and found out that the uniform doping is the most energy stable doping style. The calculated lattice parameters of bulk SnO_2 are listed in Table S2. The lattice parameters for the pure SnO_2 agree well with experimental results, and they reduce a little after Ga doping due to the smaller ionic radius of Ga. Fig. 7b-7d show the band structures and density of states (DOS) for pure SnO_2 and Ga doped SnO_2. The calculated band gap of SnO_2 is 3.43 eV, close to the experimental value of 3.597 eV. From Fig. 7, our calculation clearly revealed a gradual upward (to high energies) shift for the valence and conduction band with Sn substituted by Ga. The Fermi level shifts positively (downward) to the valence band shows there is an *p*-type doping effect when Sn substituted by Ga for SnO_2, which is attributed to that the heterovalent substitution of Sn atoms (4^+) by Ga atoms (3^+) introduces charge holes at the Ga sites. The band gap is also reduced a little when the Sn atoms are substituted by the Ga atoms (Fig. 7b). The upward shift for the conduction band minimum (CBM) is consistent with our experimental observation that the conduction band shifts negatively (upward) after Ga doping and increased V_{OC} was obtained. At the same time, the *p*-type doping effect and the reduced band gap would increase the electrical conductance, which is consistent with the increased J_{sc} when the Ga doping content is increased from 0 to 3 mol%. According to the equation $\sigma = ne\mu$ (*n* is the carrier concentration, μ is the carrier mobility), the electrical conductance of SnO_2 would be increased after Ga doping under low content, due to the increased hole concentration. However, the increasing Ga contents could also

introduce more impurity scattering centers to impede the electron transport (μ), and this effect would even dominate to reduce the whole electrical conductance when the Ga doping content exceeds some content. This is consistent with the increased electron transport time (τ_d) observed in the IMPS measurements and also accounts for the reduced J_{sc} when the Ga doping content is increased from 3 mol% to 5 mol%. It's hard to give a clear and direct relationship between the *p*-type doping effect and the suppressed charge recombination in Ga-doped SnO_2 DSSCs experimentally and theoretically. The most probable reason accounting for this is that the heterovalent Ga doping introduces charge holes (*p*-type doping) in the bulk and surface of SnO_2. These charge holes can attract electrons and act like charge trapping sites, to suppress the recombination between the electrons transferred from adsorbed dyes and the holes of the dyes and the redox mediator (I^-/I^-_3) in the electrolyte. In our previous work, the Al doping shows a more effective charge recombination suppression.[31] This is attributed to that a surface Al_2O_3 layer was formed on Al-doped SnO_2, which acts as a thin coated insulating layer and increases the interface resistance greatly to further inhibit the electron-hole recombination.

Conclusions

In summary, by introducing the rough hollow microspheres structure and Ga-doping technique, the highest power conversion efficiency (η) up to 7.11% is obtained, which is larger than that for our previous Al-doped SnO_2 DSSCs (6.91 %) and one of the highest overall photoconversion efficiency for SnO_2 based DSSCs. The Ga-doping results in a negative shift of the CB and the reduction of charge recombination so as to significantly enhance J_{sc} and V_{oc}. The highest power conversion efficiency (η) under AM1.5 simulated solar illumination (100 mW cm^{-2}) is obtained at the Ga doping amount of 3 mol%. These findings provide a new route to enhance the performance of DSSCs by

improving the two key factors, such as to tune the energy levels of SnO_2 and to retard charge recombination.

Acknowledgements

This research was supported by Shenzhen Science and Technology Research Grant (No. ZDSY20130331145131323, JCYJ20120614150201123, SGLH20120928095706623 and JCYJ20120614150338154), National Natural Science Foundation of China (Grant No. 51303186), and National Research Fund for Fundamental Key Project (2012CB932903). Additionally, we acknowledge the support of ShenZhen National Super Computing Center.

Notes and references

†Electronic Supplementary Information (ESI) available: Mott-Schottky plots of the SnO_2 and the Ga-doped SnO_2 films. Diffuse reflectance spectra of the photoelectrodes with nano SnO_2, nano hollow SnO_2 and nano hollow $Sn_{0.97}Ga_{0.03}O_2$. Specific resistivity as a function of doping level for $Sn_{1-x}Ga_xO_2$ films. Normalized device performance under constant illumination for 100 h measured in air. Elemental mapping of the $Sn_{0.97}Ga_{0.03}O_2$. Calculated total and orbital resolved densities of states for the pure SnO_2 and 6.25% Ga doped SnO_2. The reported high values of η obtained in the DSSCs based on different SnO_2 photoanode structures. Calculated structural parameters a and c for pure SnO_2 and 6.25% Ga doped SnO_2.

References

1. J. Preat, D. Jacquemin and E. A. Perpete, *Energy Environ. Sci.*, 2010, **3**, 891-904.

2. A. Hagfeldt, G. Boschloo, L. Sun, L. Kloo and H. Pettersson, *Chem. Rev.*, 2010, **110**, 6595-6663.

3. A. Yella, H. W. Lee, H. N. Tsao, C. Yi, A. K. Chandiran, M. K. Nazeeruddin, E. W. G. Diau, C. Y. Yeh, S. M.

Zakeeruddin and M. Grätzel, *Science*, 2011, **334**, 629-634.

4. W. Guo, Y. Shen, L. Wu, Y. Gao and T. Ma, *J. Phys. Chem. C*, 2011, **115**, 21494-21499.
5. K. Park, Q. Zhang, B. B. Garcia, X. Zhou, Y. H. Jeong and G. Cao, *Adv. Mater.*, 2010, **22**, 2329-2332.
6. J. Xiao, Q. Huang, J. Xu, C. Li, G. Chen, Y. Luo, D. Li and Q. Meng, *J. Phys. Chem. C*, 2014, **118**, 4007-4015.
7. J. Huo, Y. Hu, H. Jiang, W. Huang and C. Li, *J. Mater. Chem. A*, 2014, **2**, 8266-8272.
8. F. Lenzmann, J. Krueger, S. Burnside, K. Brooks, M. Gratzel, D. Gal, S. Ruhle and D. Cahen, *J. Phys. Chem B.*, 2001, **105**, 6347-6352.
9. Z. D. Li, Y. Zhou, J. Y. Zhang, W. G. Tu, Q. Liu, T. Yu and Z. G. Zou, *Cryst. Growth. Des.*, 2012, **12**, 1476-1481.
10. Y. Furubayashi, T. Hitosugi and Y. Yamamoto, *Appl. Phys. Lett.*, 2005, **86**, 252101.
11. J. F. Qian, P. Liu, Y. Xiao, Y. Jiang, Y. L. Cao, X. P. Ai and H. X. Yang, *Adv. Mater.*, 2009, **21**, 3663.
12. M. K. I. Senevirathna, P. Pitigala, E. V. A. Premalal, K. Tennakone, G. R. A. Kumara and A. Konno, *Sol. Energy Mat. Sol. C*, 2007, **91**, 544-547.
13. H. C. Pang, H. B. Yang, C. X. Guo and C. M. Li, *ACS Appl. Mater. Inter.*, 2012, **4**, 6261-6265.
14. M. H. Kim and Y. U. Kwon, *J. Phys. Chem. C*, 2011, **115**, 23120-23125.
15. E. Ramasamy and J. Lee, *J. Phys. Chem. C*, 2010, **114**, 22032-22037.
16. S. Gubbala, V. Chakrapani, V. Kumar and M. K. Sunkara, *Adv. Funct. Mater.*, 2008, **18**, 2411-2418.
17. X. C. Dou, D. Sabba, N. Mathews, L. H. Wong, Y. M. Lam and S. Mhaisalkar, *Chem. Mater.*, 2011, **23**, 3938-3945.
18. K. Perera, S. G. Anuradha, G. R. A. Kumara, M. L. Paranawitharana, R. M. G. Rajapakse and H. M. N. Bandara, *Electrochim. Acta*, 2011, **56**, 4135-4138.
19. P. Docampo, P. Tiwana, N. Sakai, H. Miura, L. Herz, T. Murakami and H. J. Snaith, *J. Phys. Chem. C*, 2012, **116**, 22840-22846.
20. C. T. Gao, X. D. Li, B. G. Lu, L. L. Chen, Y. Q. Wang, F. Teng, J. T. Wang, Z. X. Zhang, X. J. Pan and E. Q. Xie, *Nanoscale*, 2012, **4**, 3475-3481.
21. H. Wang, B. Li, J. Gao, M. Tang, H. B. Feng, J. H. Li and L. Guo, *Crystengcomm*, 2012, **14**, 5177-5181.
22. Y. F. Wang, K. N. Li, C. L. Liang, Y. F. Hou, C. Y. Su and D. B. Kuang, *J. Mater. Chem.*, 2012, **22**, 21495-21501.
23. P. N. Zhu, M. V. Reddy, Y. Z. Wu, S. J. Peng, S. Y. Yang, A. S. Nair, K. P. Loh, B. V. R. Chowdari and S. Ramakrishna, *Chem. Commun.*, 2012, **48**, 10865-10867.
24. R. Kasaudhan, H. Elbohy, S. Sigdel, Q. Hui, W. Qufu and Q. Qiquan, *Electron. Device Lett., IEEE* 2014, **35**, 578-580.
25. X. Zou, X. Liu, C. Wang, Y. Jiang, Y. Wang, X. Xiao, J. C. Ho, J. Li, C. Jiang, Q. Xiong and L. Liao, *ACS Nano*, 2012, **7**, 804-810.

26. Q. Zhao, P. Wu, B. L. Li and E. Y. Jiang, *Phys. Rev. B: Condens. Matter.* 2012, **407**, 171-174.

27. S. H. Park, J. B. Park and P. K. Song, *Curr. Appl. Phys.* 2010, **10**, S488-S490.

28. X. Lü, X. Mou, J. Wu, D. Zhang, L. Zhang, F. Huang, F. Xu and S. Huang, *Adv. Funct. Mater.* 2010, **20**, 509-515.

29. K. P. Wang and H. Teng, *Phys. Chem. Chem. Phys.* 2009, **11**, 9489-9496.

30. J. J. Teh, S. L. Ting, K. C. Leong, J. Li and P. Chen, *ACS Appl. Mater. Inter.*, 2013, **5**, 11377-11382.

31. Y. Duan, J. Zheng, N. Fu, Y. Fang, T. Liu, Q. Zhang, X. Zhou, Y. Lin and F. Pan, *J. Mater. Chem. A,* 2015, **3**, 3066-3073

32. P. Bonhôte, A. P. Dias, N. Papageorgiou, K. Kalyanasundaram and M. Grätzel, *Inorg. Chem.*, 1996, **35**, 1168-1178.

33. P. E. Blochl, *Phys. Rev. B*, 1994, **50**, 17953-17979.

34. G. Kresse and D. Joubert, *Phys. Rev. B*, 1999, **59**, 1758-1775.

35. J. Heyd, G. E. Scuseria and M. Ernzerhof, *J. Chem. Phys.,* 2003, **118**, 8207.

36. J. Heyd, G. E. Scuseria and M. Ernzerhof, *J. Chem. Phys.*, 2006, **124**, 219906.

37. G. Kresse and J. Furthmuller, *Phys. Rev. B*, 1996, **54**, 11169-11186.

38. G. Kresse and J. Furthmuller, *Comput. Mater. Sci.*, 1996, **6**, 15-50.

39. J. Paier, M. Marsman, K. Hummer, G. Kresse, I. C. Gerber and J. G. Ángyán, *J. Chem. Phys.*, 2006, **124**, 154709.

40. J. P. Perdew, K. Burke and M. Ernzerhof, *Phys. Rev. Lett.*, 1996, **77**, 3865-3868.

41. J. B. Varley, A. Janotti and C. G. Van de Walle, *Phys. Rev. B*, 2010, **81**, 245216.

42. D. O. Demchenko, B. Earles, H. Y. Liu, V. Avrutin, N. Izyumskaya, Ü. Özgür, and H. Morkoç, *Phys. Rev. B*, 2011, **84**, 075201.

43. T. L. Barr, M. A. Lishka, L. M. Chen and M. Mohsenian, *J. Am. Chem. Soc.*, 1988, **110**, 7962-7975.

44. J. Li and H. C. Zeng, *J. Am. Chem. Soc.,* 2007, **129**, 15839-15847.

45. K. Tasaki, A. Goldberg and M. Winter, *Electrochim. Acta*, 2011, **56**, 10424-10435.

46. J. Xing, W. Q. Fang, Z. Li and H. G. Yang, *Ind. Eng. Chem. Res.*, 2012, **51**, 4247–4253

47. S. Yang, Y. Hou, Jun Xing, B. Zhang, F. Tian, X. H. Yang and H. G. Yang, Chem. Eur. J., 2013, **19**, 9366–9370

48. R. Katoh and A. Furube, J. Photochem. Photobiol., C, 2014, **20**, 1-16.

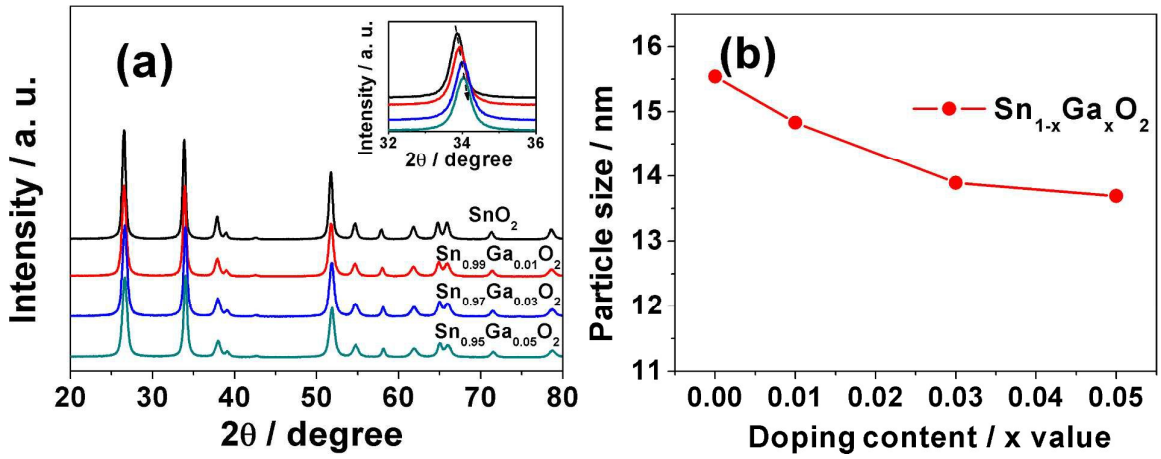

Fig. 1. (a) XRD patterns of SnO_2 and Ga-doped SnO_2; (b) Plots of doping content vs. particle size, derived using the Scherrer equation.

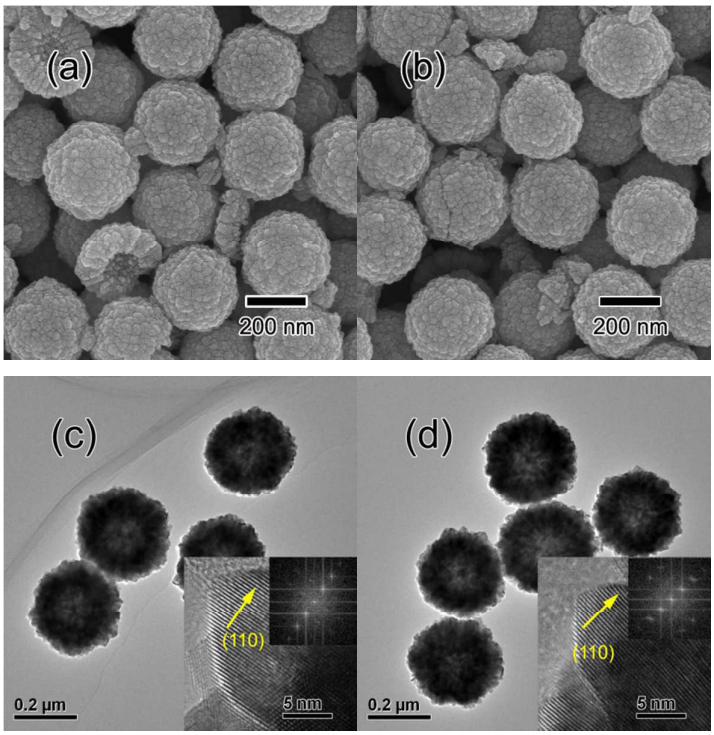

Fig. 2. SEM images of (a) SnO_2, and (b) $Sn_{0.98}Ga_{0.03}O_2$. TEM, HR-TEM and FFT (inset) images of (c) SnO_2, and (d) $Sn_{0.97}Ga_{0.03}O_2$.

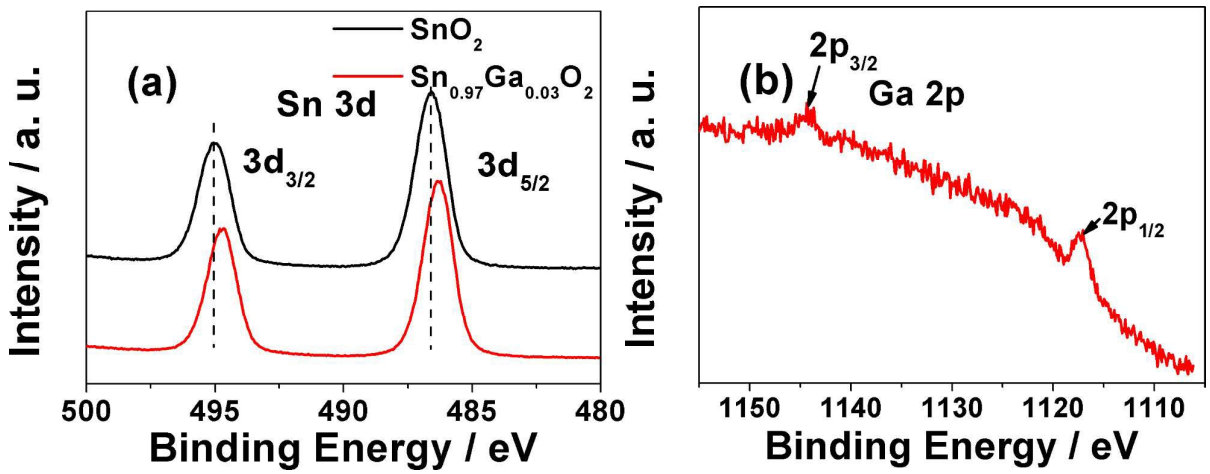

Fig. 3. X-ray photoelectron spectra of the $Sn_{0.97}Ga_{0.03}O_2$ sample: (a) Sn 3d, (b) Ga 2p.

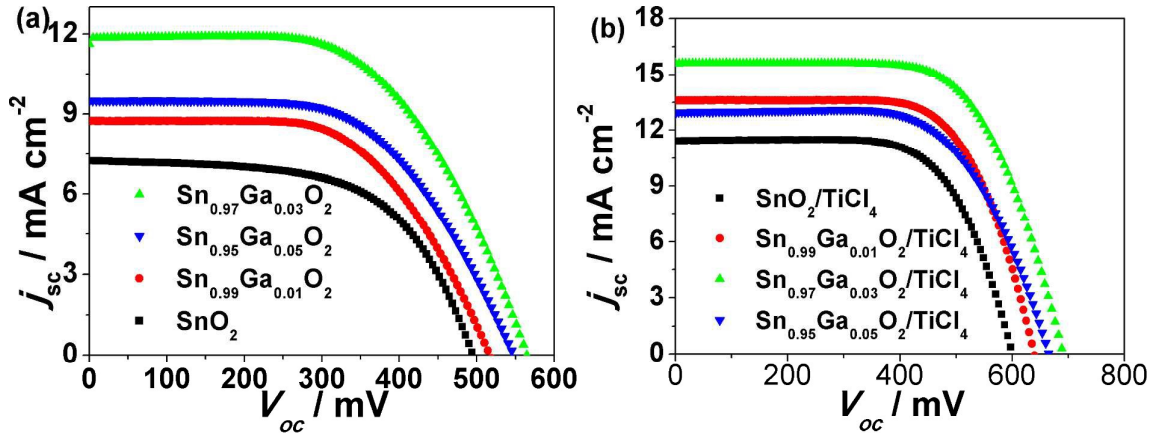

Fig. 4. (*J-V*) curves measured for SnO_2 and Ga-doped SnO_2 photoanodes sensitized with N3 dye.

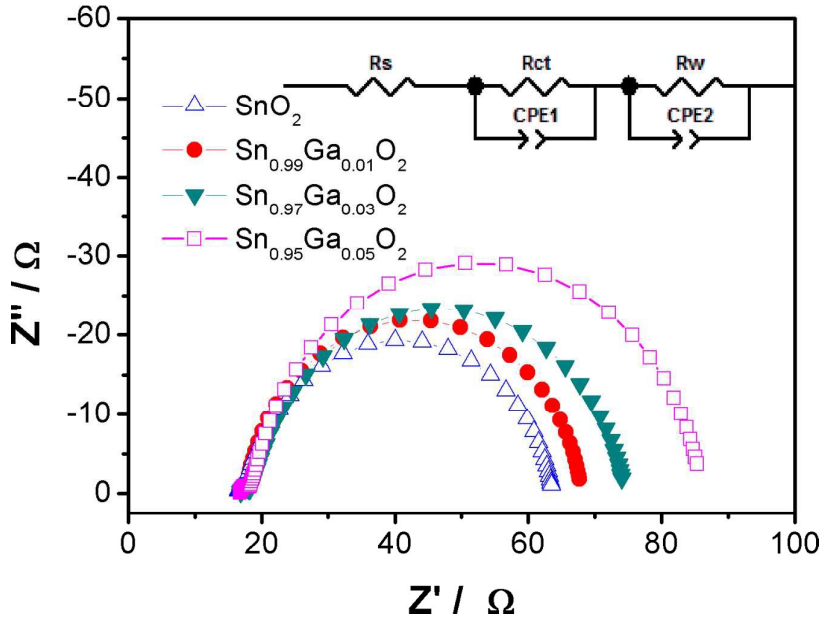

Fig. 5. Nyquist plots of the cells with electrodes at open circuit. Inset shows the corresponding equivalent circuit.

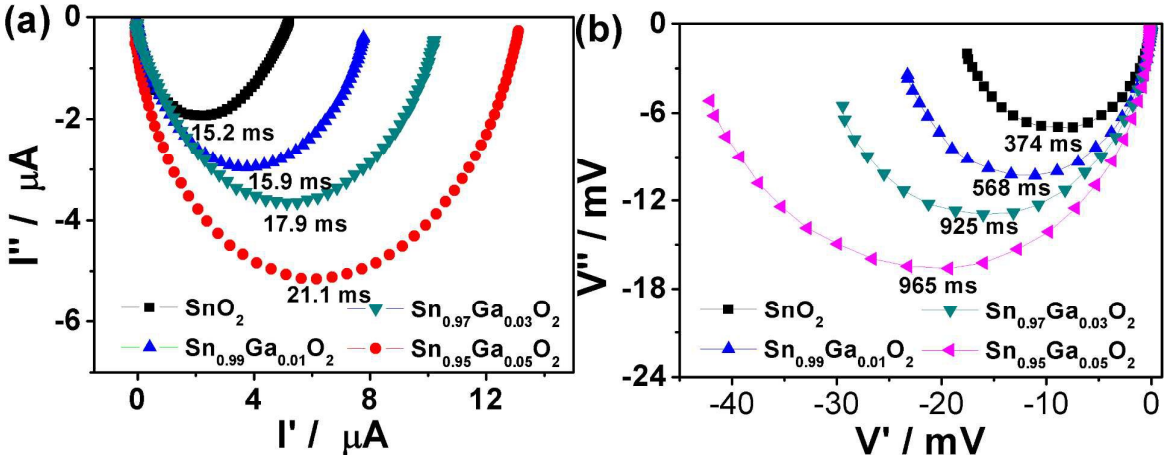

Fig. 6. Complex plane plots and the corresponding time constant of the pure-SnO_2 and Ga-doped SnO_2 cells obtained from (a) IMPS and (b) IMVS.

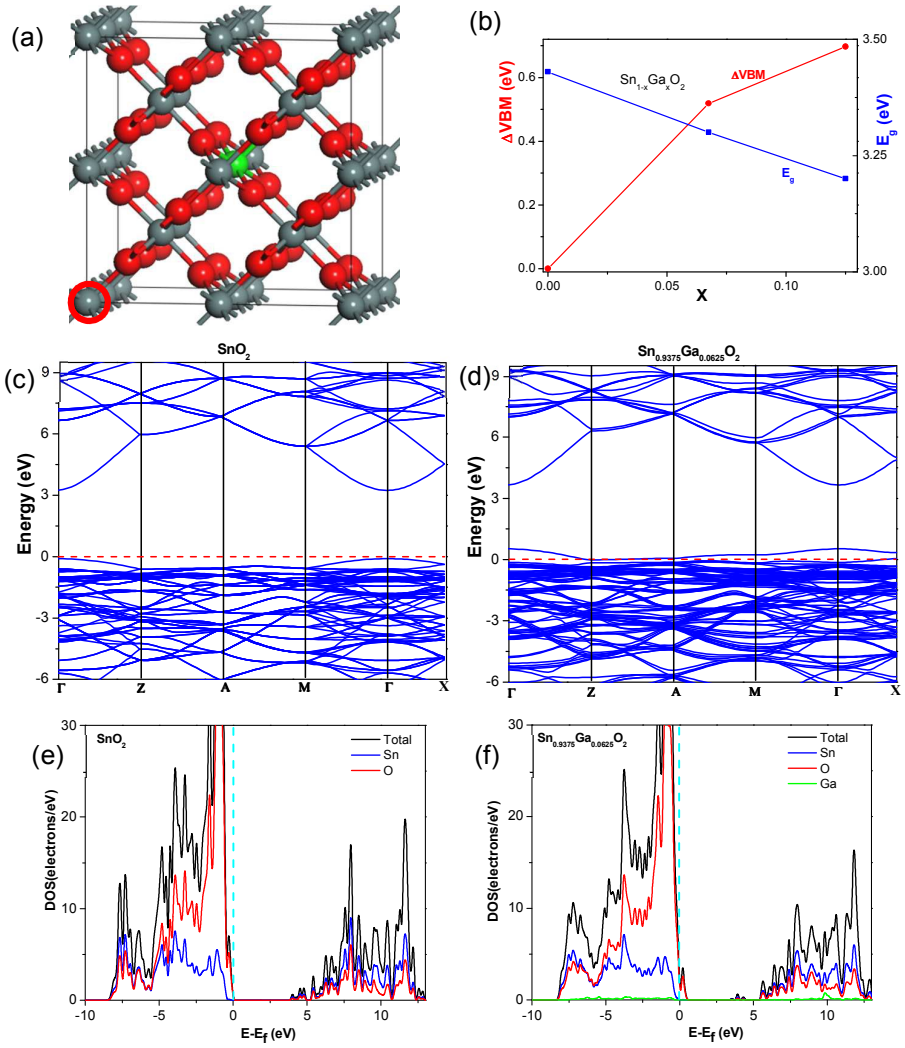

Fig. 7. (a) Configurations of $Sn_{0.9375}Ga_{0.0625}O_2$. Grey ball: Sn; Green ball: Ga; red ball: O. (b) Valance band maximum (VBM) shift (red line) and variation of the band gap (blue line) as a function of the level of Sn substitution by Ga. The Fermi level is set to zero. (c) and (d) Band structures for the pure SnO_2 and 6.25 mol% Ga doped SnO_2. The Fermi level is set to zero. (e) and (f) Total and projected density of states for the pure SnO_2 and 6.25mol% Ga doped SnO_2. The Fermi level is set to zero. The vertical dashed line denotes the Fermi level.

Table 1 Evolution of cell characteristics for SnO_2 and Ga-doped SnO_2 films, with and without $TiCl_4$ post-treatment. All data presented are average data obtained from 5 Cells.

	J_{SC} (mA cm^{-2})	V_{OC} (mV)	η (%)	FF	Dye loading ($\times 10^{-7}$ mol cm^{-2})
nano-SnO_2[a]Ref. 31	7.92	467	2.03	0.55	0.77
SnO_2	7.23	496	2.13	0.60	0.62
$Sn_{0.99}Ga_{0.01}O_2$	8.73	517	2.68	0.60	0.70
$Sn_{0.97}Ga_{0.03}O_2$	11.62	565	3.84	0.59	0.74
$Sn_{0.95}Ga_{0.05}O_2$	9.50	547	2.96	0.57	0.76
$SnO_2/TiCl_4$	11.42	601	4.67	0.68	0.93
$Sn_{0.99}Ga_{0.01}O_2/TiCl_4$	13.59	640	5.91	0.68	1.06
$Sn_{0.97}Ga_{0.03}O_2/TiCl_4$	15.61	691	7.11	0.66	1.11
$Sn_{0.95}Ga_{0.05}O_2/TiCl_4$	12.90	665	5.49	0.64	1.13

[a]Ref. 31

Table 2 BET specific surface area (SSA) of the as synthesized samples determined from N_2 sorption analysis.

Sample	BET SSA (m^2 g^{-1})
SnO_2	21.48
$Sn_{0.99}Ga_{0.01}O_2$	25.15
$Sn_{0.97}Ga_{0.03}O_2$	28.55
$Sn_{0.95}Ga_{0.05}O_2$	30.14